nature communications

Article

https://doi.org/10.1038/s41467-025-67445-6

VPS13B recruits lipid vesicles to promote mitochondrial fission and quality control

Received: 6 October 2024

Accepted: 1 December 2025

Published online: 16 December 2025

Check for updates

Soo-Kyeong Lee[1,4], Hyun-Ji Ham[1,4], Semin Park[1,4], Hye Eun Lee[2], Ji Young Mun[2], Deok-Jin Jang[3] ✉ & Jin-A Lee[1] ✉

Mutations in the gene VPS13B, which encodes a Golgi-associated protein, cause the neurodevelopmental disorder Cohen syndrome, but the protein's function is unclear. Here we show that this protein is essential for mitochondrial morphology and quality control. Cells lacking VPS13B, including neurons derived from Cohen syndrome patients, exhibit abnormally elongated and fused mitochondria with reduced membrane potential and impaired mitophagy. Mechanistically, the protein localizes to Mitofusin 2-positive mitochondria via its C-terminal region and recruits phosphatidylinositol-4-phosphate-rich Golgi vesicles to mitochondrial fission sites. Loss of VPS13B or depletion of phosphatidylinositol-4-phosphate results in incomplete mitochondrial fission despite normal recruitment of Dynamin-related protein 1, indicating that lipid transfer by VPS13B is required for membrane fission. VPS13B links Golgi-derived lipid vesicles to the mitochondrial fission machinery, ensuring proper mitochondrial fission and quality control and potentially explaining the mitochondrial defects in Cohen syndrome.

The VPS13 (Vacuolar Protein Sorting 13) family of proteins consists of highly conserved, large proteins that regulate various cellular processes. In yeast (*Saccharomyces cerevisiae*), a single protein, VPS13, was initially identified in a screen for proteins involved in vacuolar protein sorting[1,2]. Subsequently, VPS13 has been extensively characterized as a multifunctional protein involved in protein trafficking, vesicular transport and fusion, sporulation, mitochondrial homeostasis, phagocytosis, and autophagy in yeast and other lower eukaryotic organisms[3–5]. More recent studies have shown that VPS13 family proteins mediate non-vesicular lipid transport at intracellular membrane contact sites[6–9].

In humans, there are four paralogs (VPS13A, B, C, and D) of yeast VPS13, and these proteins are highly conserved across species from yeast to humans[1,7,10,11]. Notably, genetic mutations in human VPS13 genes are strongly associated with several genetic disorders, including neurodevelopmental and neurodegenerative diseases. These include Chorea-acanthocytosis (VPS13A), Cohen syndrome (CS; a condition characterized by global developmental delay and intellectual disability (VPS13B)), an early-onset form of Parkinson's disease (VPS13C), and a form of Ataxia with spasticity (VPS13D)[7,12–21].

Among these paralogs, VPS13B, also known as CS-associated protein (COH1), is known to regulate Golgi integrity, glycosylation, and neurite outgrowth through its interaction with the RAB6 GTPase[16,22,23]. More recently, VPS13B has been reported to control acrosome biogenesis by modulating Golgi dynamics and membrane trafficking[14]. Recent studies have shown that small GTPases and phosphoinositides interact with soluble N-ethylmaleimide-sensitive-factor attachment protein receptor (SNARE) proteins to target VPS13B, which regulates targeting via Stx6 and Stx13, functioning as a regulatory factor in transport from early endosomes to recycling endosomes[24]. Additionally, VPS13B has been reported to localize to and promote the formation of Golgi-lipid droplet (LD) contacts upon oleic acid (OA) stimulation, suggesting a potential role for VPS13B-mediated cellular contacts[25]. Moreover, recent studies suggest that VPS13B may facilitate

[1]Department of Biological Sciences and Biotechnology, College of Life Sciences and Nanotechnology, Hannam University, Daejeon, South Korea. [2]Neural circuit research group, Korea Brain Research Institute, Daegu, South Korea. [3]Department of Ecological Science, College of Ecology and Environment, Kyungpook National University, Sangju, South Korea. [4]These authors contributed equally: Soo-Kyeong Lee, Hyun-Ji Ham, Semin Park.
✉e-mail: jangdj@knu.ac.kr; leeja@hnu.kr

bulk lipid transport to expand Golgi membranes, with FAM177A1 possibly assisting in this function[9]. While its cellular roles in the Golgi complex and endosomes have been reported using RNAi-based studies in mammalian cell lines[14,24], the precise functions of VPS13B in knockout (KO) cells remain poorly understood. Furthermore, although evidence increasingly supports the role of VPS13B in the regulation of Golgi complexes, little is known about its role in regulating other organelles, such as mitochondria.

In this study, we demonstrate that VPS13B regulates mitochondrial dynamics and quality control. In VPS13B KO cells and Cohen syndrome patient-derived iPSC-induced neurons, VPS13B loss causes mitochondrial hyperfusion, decreased membrane potential, and impaired PINK1/Parkin-mediated mitophagy. Upon mitochondrial stress, endogenous VPS13B is recruited via a C-terminal MLD—necessary and sufficient for targeting—to Mfn2-positive mitochondria contacts, where it accumulates at Drp1-positive fission site and promotes delivery of phosphatidylinositol 4-phosphate (PI4P)-enriched Golgi vesicles. VPS13B loss or acute PI4P depletion lowers fission rates and stalls fission without affecting Drp1 recruitment or phosphorylation, placing the PI4P-VPS13B axis downstream of Drp1 to facilitate late-stage membrane severing. Neurons derived from patients with Cohen syndrome phenocopy these defects—hyperfused networks, decreased membrane potential, reduced Drp1 localization, and increased PINK1—underscoring clinical relevance. Thus, VPS13B acts as a Golgi–mitochondria association that couples PI4P-vesicle supply to the fission machinery to sustain mitochondrial fission and mitophagy.

Results

VPS13B KO leads to hyperfused mitochondria

To investigate the specific roles of VPS13B associated with CS, we first assessed the cellular localization of VPS13B in wild-type (WT) cells. Consistent with previous reports[17], VPS13B was predominantly co-localized to Galatosyltransferase (GalT) (Supplementary Fig. 1a) and TGN46 (Supplementary Fig. 1b), the Trans-Golgi Network (TGN) marker, indicating the Golgi apparatus localization[17]. Normally, other VPS13 isoforms, including VPS13A, C, and D, are localized to the ER via the phenylalanine-phenylalanine-acidic-tract (FFAT) motif-dependent ER protein VAP[7,26–28]. Interestingly, VPS13B is the only isoform without an FFAT motif, and is consistently localized to the Golgi, not the ER.

Next, to examine the roles of VPS13B resulting from its loss of function in cells, we generated VPS13B KO cells using CRISPR/Cas9 technology[21,29]. The gene sequencing results, and Western blot analysis and immunocytochemistry with an anti-VPS13B antibody confirmed the absence of VPS13B at the protein and cellular levels (Supplementary Fig. 1c–e). To delve deeper into the relevance of cellular organelle defects in VPS13B deficiency, VPS13B KO cells were transfected with marker proteins for various organelles EGFP-tagged Rab5 (early endosome), Rab7 (late endosome), Sec61 (ER), GalT (Golgi apparatus), LAMP1 (lysosome), and mRFP-TOM20 (mitochondria, pseudo-colored green) (Supplementary Fig. 1f). Intriguingly, organelles marked by Rab5, Rab7, Rab9, or LAMP1 showed a scattered distribution in WT cells, but were clustered near the nucleus in VPS13B KO cells, underscoring VPS13B's role in vesicular trafficking[16,30]. In addition to the qualitative observation of Golgi fragmentation, quantitative analysis by endogenous Golgi staining using anti-TGN46 antibody revealed that VPS13B KO cells exhibited a significant increase in the number of discrete TGN structures, while the average area and perimeter of individual TGNs were reduced and circularity values were elevated (Supplementary Fig. 1g, h), indicating that VPS13B deficiency leads to fragmentation, resulting in more numerous, smaller, and morphologically rounder Golgi elements compared to WT. Notably, VPS13B KO cells displayed markedly elongated and interconnected mitochondria, indicative of hyperfusion and suggesting a critical role for VPS13B in maintaining mitochondrial morphology (Supplementary Fig. 1f).

Regarding the skeletonized TOM20-positive mitochondria, we observed that the structures in VPS13B KO cells appeared more interconnected compared to WT cells (Fig. 1A). To quantify this morphological change, we measured the area and perimeter of individual mitochondria. This analysis revealed a significant increase in both mitochondrial area and perimeter in VPS13B KO cells (Fig. 1B, C), indicating a hyperfused mitochondrial morphology.

To further investigate the abnormal mitochondrial morphology observed under confocal microscopy, we performed electron microscopy (EM) analysis to assess at the ultrastructural level. The EM analysis revealed that, in contrast to the typical morphology of mitochondria in WT cells, mitochondria in VPS13B KO cells were frequently branched and elongated (Fig. 1D). This altered morphology corresponded to a significant increase in both the average mitochondrial area and perimeter compared to WT controls (Fig. 1E, F). This analysis revealed a significant increase in both the average mitochondrial area and perimeter in VPS13B KO cells compared to WT controls, indicating that the absence of VPS13B leads to distinct, enlarged changes in mitochondrial structure.

Given that VPS13B deficiency leads to abnormal mitochondrial morphology, we next asked whether VPS13B is associated with mitochondria and which domain mediates this interaction. To this end, we mapped VPS13B's C-terminus, which contains a conserved DH-like domain–pleckstrin homology (DHL-PH) region and a Mitochondria-Associated Membrane (MAM) localization domain (MLD)-like segment with homology to the C-terminus of ATG2A (reported to mediate MAM targeting)[31]. We generated EGFP-tagged constructs comprising an MLD-deletion mutant (ΔMLD), and C-terminal fragments encompassing the DHL-PH region (amino acids 3500-3997) or the isolated MLD (amino acids 3662-3793)[7,9,31–33] (Fig. 1G). VPS13B-full-length (FL)-EGFP exhibited clear enrichment at TOM20-positive mitochondria, and both EGFP-VPS13B-DHL-PH and EGFP-VPS13B-MLD similarly co-localized with mitochondrial markers, indicating that the C-terminal MLD-containing region is sufficient for mitochondrial targeting (Fig. 1H). In contrast, VPS13B-ΔMLD-EGFP failed to accumulate at mitochondria, demonstrating that the MLD is necessary for VPS13B's mitochondrial localization (Fig. 1H).

To further assess whether VPS13B is involved at Mfn2-positive mitochondria contact sites (MAM)[31,34,35], we performed in situ proximity ligation assays (PLA) using antibodies against endogenous VPS13B and Mitofusin-2 (Mfn2), a marker/tether enriched at Mfn2-positive mitochondria interfaces[34,35]. Because PLA detects protein proximity within ~40 nm, it provides a sensitive readout of residency at contact sites[36]. In WT cells, we observed abundant VPS13B-Mfn2 PLA puncta that aligned with mitochondrial profiles, whereas VPS13B KO cells showed signals near background (Fig. 1I, J). Notably, re-expression of VPS13B-FL-EGFP in KO cells restored the VPS13B (using GFP antibodies)-Mfn2 PLA signal, while VPS13B-ΔMLD-EGFP did not exhibit such localization(Fig. 1I, J). These results demonstrate that VPS13B localizes to Mfn2-positive mitochondria in an MLD-dependent manner.

To confirm that the hyperfused mitochondrial phenotype results directly from VPS13B loss and depends on its mitochondrial association, we performed a rescue experiment by overexpression. Rescue of VPS13B-KO cells with VPS13B-FL-EGFP, but not with VPS13B-ΔMLD-EGFP, normalized mitochondrial morphology to that of wild-type cells (Fig. 1K, L). These results demonstrate that the hyperfused phenotype is a direct consequence of VPS13B loss and that MLD-dependent mitochondrial association of VPS13B is critical for the maintenance of mitochondrial architecture. Our findings indicate that the Golgi-associated protein VPS13B is essential for maintaining mitochondrial morphology, and that its loss leads to abnormal mitochondrial structure, highlighting a critical link between VPS13B and mitochondrial regulation.

https://doi.org/10.1038/s41467-025-67445-6

Loss of VPS13B causes mitochondrial depolarization and defective dynamics

Given that the abnormal mitochondrial morphology observed in VPS13B-deficient cells could alter mitochondrial physiology, we first assessed mitochondrial membrane potential (ΔΨm). We measured ΔΨm using tetramethylrhodamine methyl ester (TMRM) together with MitoTracker to delineate mitochondrial area, quantifying ΔΨm as integrated TMRM fluorescence normalized to the MitoTracker-positive

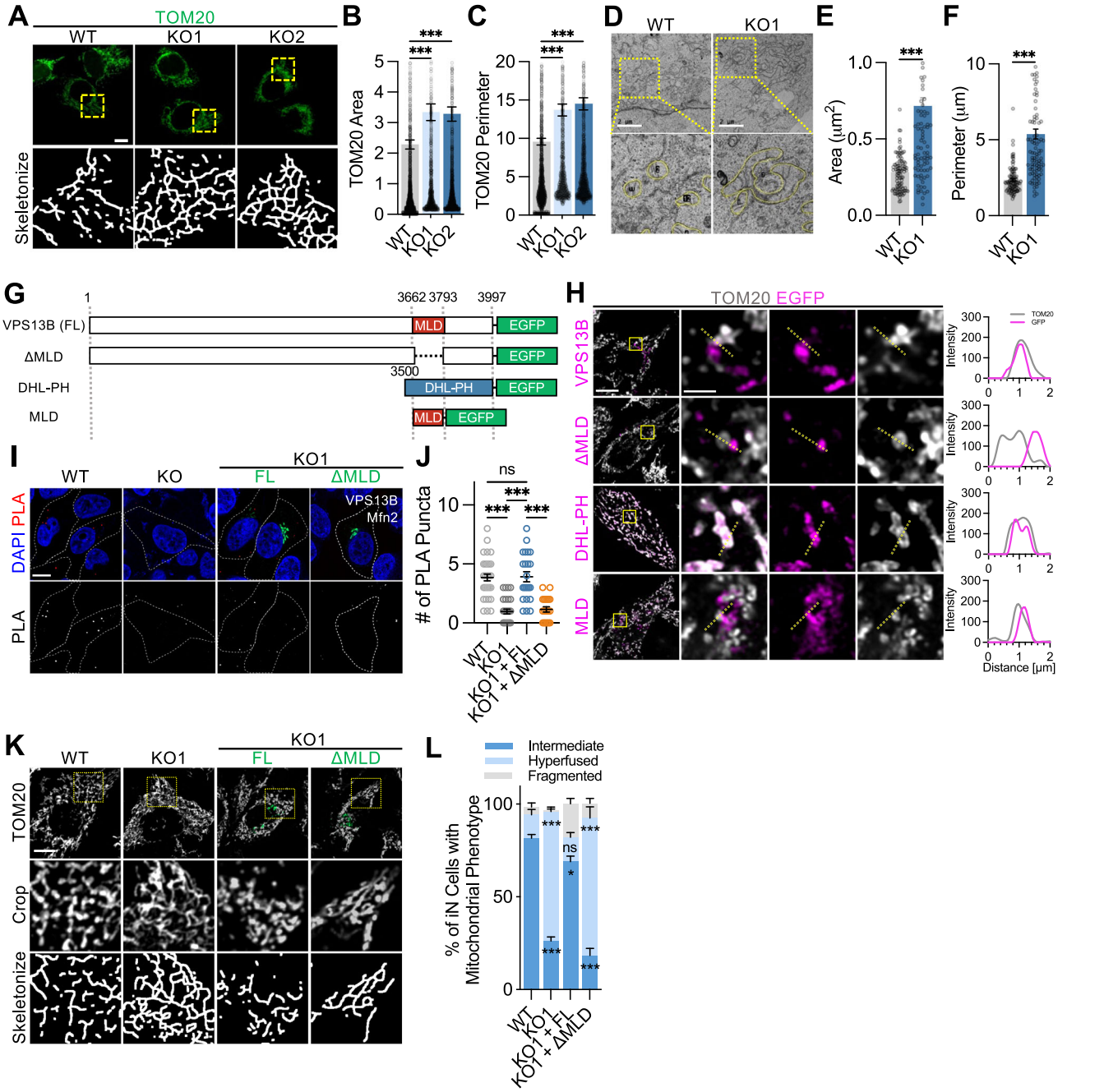

Fig. 1 | VPS13B regulates mitochondrial morphology and quality control. **A** Representative confocal images of wild-type (WT) and *VPS13B* knockout (KO) HeLa cells immunostained for TOM20 with DAPI. Scale bars, 10 μm. (B, C) Quantification of mitochondrial Area (**B**) and Perimeter (**C**). Analysis via Kruskal-Wallis with Dunn's test; ***$p < 0.001$. WT; $n = 25$, KO1; $n = 25$, KO2; $n = 25$ cells. All data are obtained from 5 independent experiments. **D** Transmission electron microscopy (TEM) images of WT and KO1 cells. Scale bar, 2 μm. **E**, **F** Quantification of mitochondrial Area (**E**) and Perimeter (**F**). Analysis via two-tailed Mann-Whitney test; ***$p < 0.001$. WT; $n = 106$, KO1; $n = 99$ mitochondria. All data are obtained from 2 independent experiments. **G** Schematic model of VPS13B domains: full-length(FL), ΔMLD, DHL-PH, and MLD. DHL-PH: DH-like domain and pleckstrin homology domain, MLD: Mitochondria-Localization Domain. **H** Confocal images of WT cells expressing EGFP-tagged VPS13B constructs (magenta) stained for TOM20 (gray). Lines indicate scan analysis path. Data are representative of 3 independent experiments. Scale bars, 10 μm. **I** Proximity ligation assays (PLA) images of WT and KO cells expressing VPS13B-EGFP or VPS13B-ΔMLD-EGFP labeled with VPS13B, Mfn2, and GFP antibodies. Scale bars, 10 μm. **J** Quantification of PLA puncta. Analysis via Kruskal-Wallis with Dunn's test; ***$p < 0.001$, n.s. = not significant. WT; $n = 34$, KO; $n = 30$, KO + FL; $n = 23$, KO1 + ΔMLD; $n = 20$ cells. All data are obtained from 3 independent experiments. **K** Representative confocal images of WT and KO cells transfected with VPS13B-FL-EGFP and VPS13B-ΔMLD-EGFP and immunostained with TOM20 antibodies. Scale bars, 10 μm. **L** Quantification of mitochondrial morphology. Analysis via one-way ANOVA with Dunnett's test. ***$p < 0.001$, *$p = 0.02$, n.s. = not significant. WT; $n = 104$, KO; $n = 223$, KO + FL; $n = 136$, KO + ΔMLD; $n = 118$ cells. All data are obtained from 5 independent experiments. Data are presented as mean ± SEM.

https://doi.org/10.1038/s41467-025-67445-6

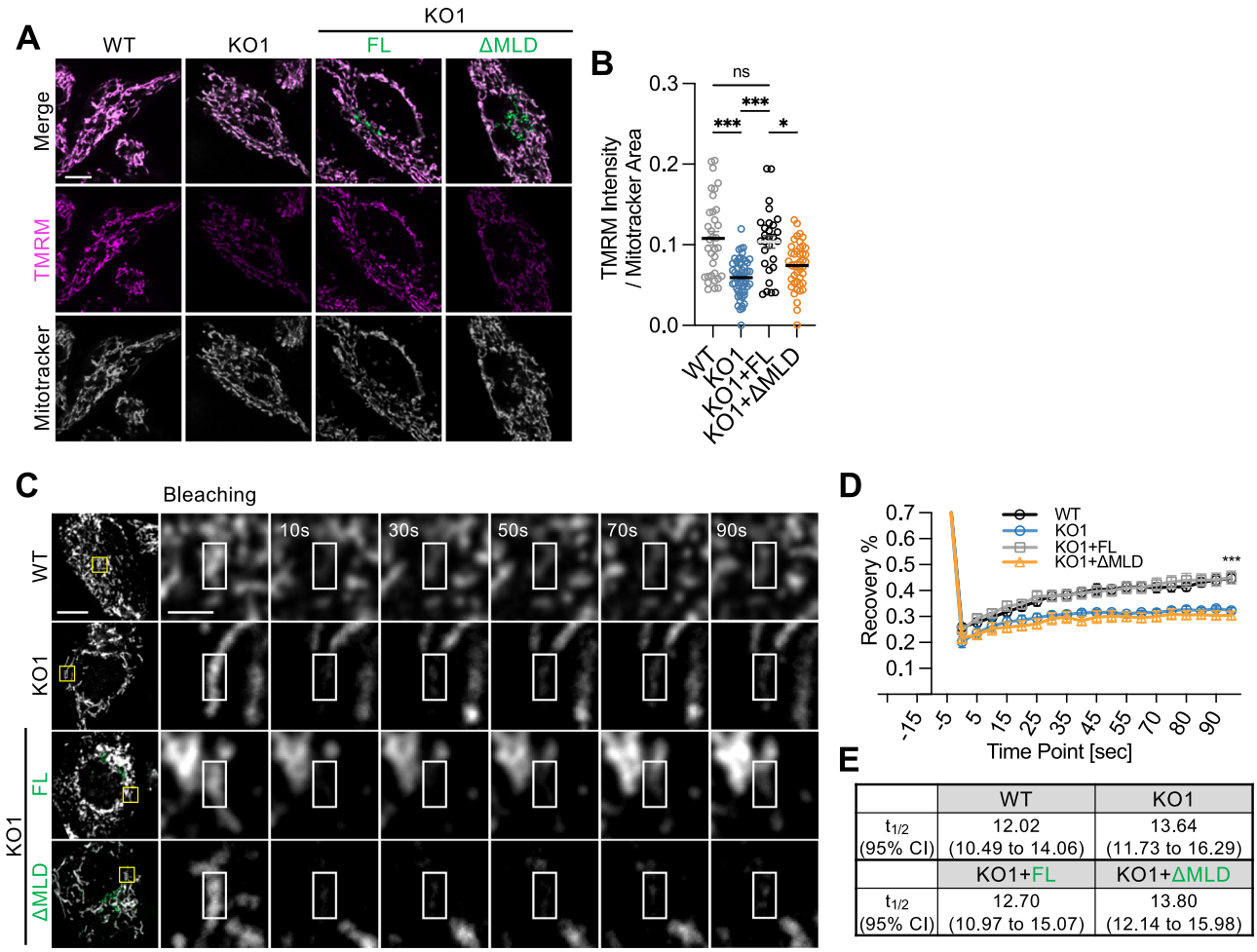

	WT	KO1
$t_{1/2}$ (95% CI)	12.02 (10.49 to 14.06)	13.64 (11.73 to 16.29)
	KO1+FL	KO1+ΔMLD
$t_{1/2}$ (95% CI)	12.70 (10.97 to 15.07)	13.80 (12.14 to 15.98)

Fig. 2 | VPS13B required for mitochondrial membrane potential and membrane dynamics. A Live-cell images of WT and KO cells transfected with VPS13B-FL-EGFP and VPS13B-ΔMLD-EGFP stained with TMRM and Mitotracker DeepRed. Scale bars, 10 μm. **B** Quantification of TMRM intensity normalized to Mitotracker area. Analysis via one-way ANOVA with Dunnett's test.***$p < 0.001$, *$p = 0.01$, n.s. = not significant. WT; $n = 34$, KO; $n = 57$, KO + FL; $n = 28$, KO + ΔMLD; $n = 43$ cells. All data are obtained from 3 independent experiments. **C** Confocal images from Fluorescence Recovery After Photobleaching (FRAP) assays of WT and KO cells transfected with VPS13B-FL-EGFP and VPS13B-ΔMLD-EGFP and mRFP-TOM20. Scale bars, 10 μm. **D** Quantitative analysis of fluorescence recovery. Analysis via Kruskal-Wallis with Dunn's test. Data are presented as mean ± SEM. WT vs. KO1, $p = 0.0451$, KO1 vs. KO1 + FL, $p = 0.0321$; KO1 + FL vs. KO1 + ΔMLD, $p = 0.0003$. WT; $n = 20$, KO1; $n = 13$, KO1 + FL; $n = 22$, KO1 + ΔMLD; $n = 21$ mitochondrial region of interests(ROIs). All data are obtained from 3 independent experiments. **E** Half-time of recovery ($t_{1/2}$) of mRFP-TOM20 calculated from one-phase association fits. Statistical significance between groups was determined by the Extra sum-of-squares F test. CI: Confidence Interval. Data are presented as mean ± SEM.

area (TMRM intensity/MitoTracker area). VPS13B KO cells showed a statistically significant reduction in this normalized ΔΨm metric compared with WT (Fig. 2A, B). Re-expression of VPS13B-FL-EGFP but not but not VPS13B-ΔMLD-EGFP in the KO cells significantly restored the normalized TMRM signal toward WT levels (Fig. 2A, B). These findings demonstrate that VPS13B deficiency leads to mitochondrial depolarization and highlights its essential role in maintaining mitochondrial bioenergetic integrity.

To further interrogate the dynamics of the hyperfused mitochondrial network, we performed a fluorescence recovery after photobleaching (FRAP) assay on cells expressing mRFP-tagged TOM20. VPS13B KO cells exhibited significantly reduced fluorescence recovery relative to WT (Fig. 2C–E), indicating diminished outer mitochondrial membrane mobility and impaired membrane dynamics consistent with a dysfunctional network architecture. Importantly, re-expression of VPS13B-FL-EGFP, but not VPS13B-ΔMLD-EGFP in the KO cells, significantly restored the recovery toward WT levels, demonstrating functional rescue and mitochondria targeting of VPS13B is essential for maintaining mitochondrial functions (Fig. 2C–E). Overall, these findings show that loss of VPS13B leads to abnormal mitochondrial morphology accompanied by functional deficits, and they are consistent with an imbalance in fusion–fission homeostasis—i.e., reduced fission efficiency and/or excessive fusion in the absence of VPS13B.

VPS13B deficiency impairs PINK1/Parkin-mitophagy

Emerging evidence highlights that damaged or abnormal mitochondria are closely linked to mitophagy activation, emphasizing the critical role of mitochondrial quality control in maintaining cellular homeostasis[37,38]. To investigate whether VPS13B loss affects mitophagy, we examined the PINK1/Parkin pathway under carbonyl cyanide m-chlorophenyl hydrazone (CCCP) treatment using the MitoQC reporter (tandem mCherry-GFP tagged to the mitochondrial targeting sequence of FIS1). Mitophagic flux was quantified as the number of mCherry-only puncta (mitolysosomes) per cell. In WT cells stably expressing Myc-Parkin, CCCP induced a robust increase in mitolysosome number, whereas VPS13B KO cells showed a statistically significant reduction and failed to mount a comparable increase (Fig. 3A, B). Importantly, re-expression of VPS13B-FL-EGFP but not VPS13B-ΔMLD-EGFP in the KO background rescued mitolysosome counts

https://doi.org/10.1038/s41467-025-67445-6

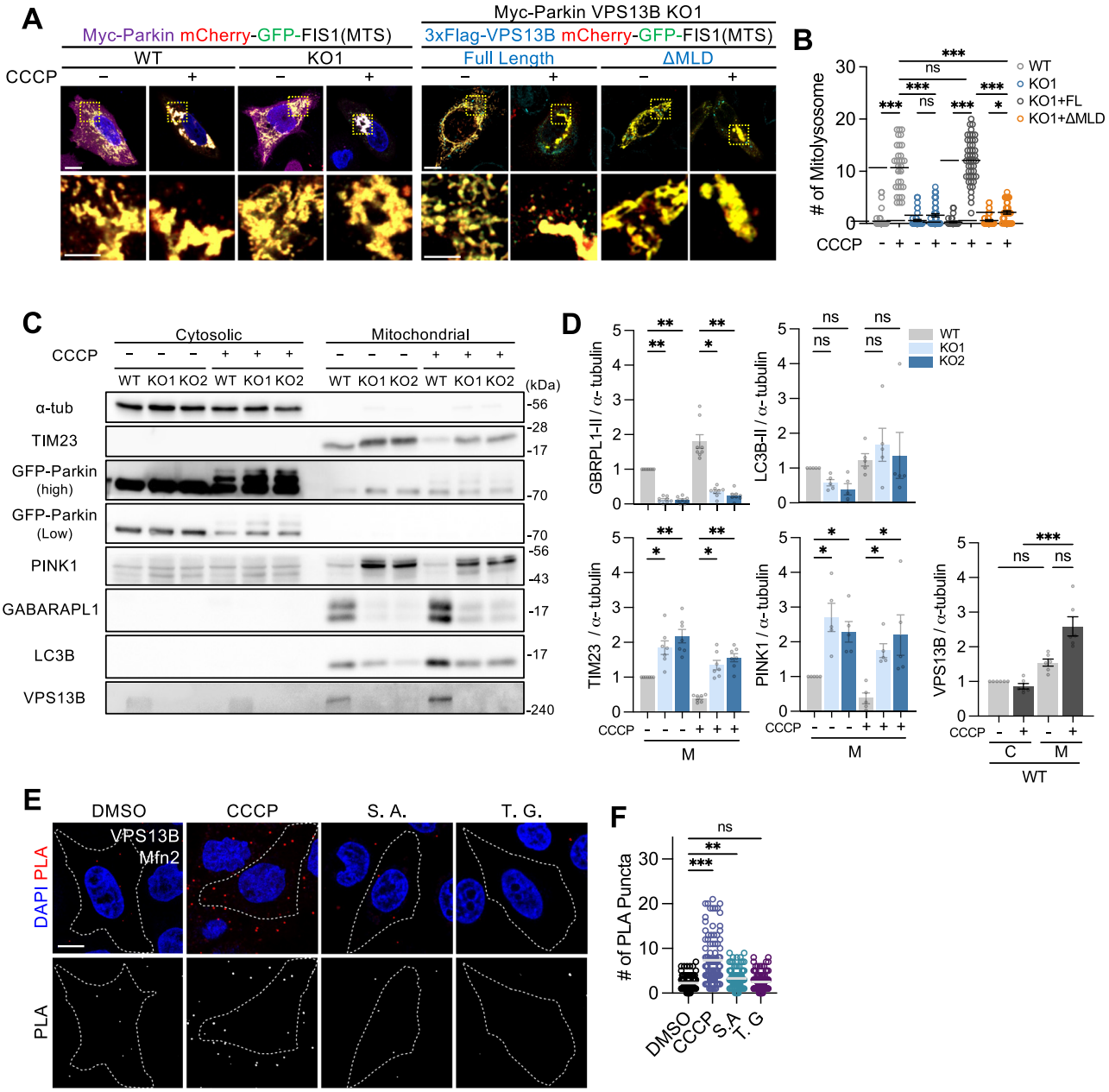

Fig. 3 | VPS13B deficiency shows impaired mitophagy. A Confocal images of WT and KO cells stably expressing Myc-Parkin and transiently expressing mCherry-GFP-FIS1 (MTS; mitochondria targeting sequence). Scale bars, 10 μm. **B** Quantification of mitolysosomes (red-only puncta) per cell. Analysis via Kruskal-Wallis with Dunn's test. ***$p < 0.001$, *$p = 0.04$, n.s. = not significant. WT CTL; $n = 52$, WT CCCP; $n = 31$, KO1 CTL; $n = 52$, KO1 CCCP; $n = 49$, KO1 + FL CTL; $n = 51$, KO1 + FL CCCP; $n = 47$, KO1 + ΔMLD CTL; $n = 48$, KO1 + ΔMLD CCCP; n = 40cells. All data are obtained from 3 independent experiments. **C** Immunoblot of mitochondrial fraction lysates from EGFP-Parkin stably expressing WT and KO cells treated with CCCP. **D** Quantification of fold changes in protein levels for each labeled protein. Analysis via Kruskal-Wallis with Dunn's test. GABARAPL1; ** $p = 0.001$, * $p = 0.03$, LC3B; n.s. = not significant, TIM23; *$p = 0.02$, **$p = 0.002$, *$p = 0.04$, **$p = 0.004$, PINK1; left to right *$p = 0.02$, 0.05, 0.04, 0.02, VPS13B; ***$p < 0.001$. All data are obtained from PINK1, LC3B; $n = 5$, GABARAPL1; $n = 8$, VPS13B; $n = 6$, TIM23; $n = 7$ independent experiments experiments per group. **E** Proximity ligation assays (PLA) images of WT cells with VPS13B and Mfn2 antibodies. Scale bars, 10 μm. **F** Quantification of PLA signal puncta. Analysis via Kruskal-Wallis with Dunn's test. ***$p < 0.001$, **$p = 0.007$, n.s. = not significant. DMSO; $n = 100$, CCCP; $n = 99$, S.A.; $n = 100$, T.G.; $n = 100$ cells. All data are obtained from 3 independent experiments. Data are presented as mean ± SEM. C: Cytosol, M: Mitochondrial.

toward WT levels (Fig. 3A, B). These results indicate that VPS13B is required for efficient PINK1/Parkin-mediated mitophagic flux.

To assess whether VPS13B participates directly in PINK1/Parkin-mediated mitophagy, we fractionated cytosolic and mitochondrial pools from WT and VPS13B KO cells in the presence or absence of CCCP conditions and immunoblotted for EGFP-Parkin, PINK1, GABARAPL1, LC3B, p62, and VPS13B. In WT cells, CCCP elicited a robust increase of VPS13B in the mitochondrial fraction, indicating stress-induced recruitment to damaged mitochondria (Fig. 3C, D). Concomitantly, LC3B and GABARAPL1 were enriched in the mitochondrial fraction of WT upon CCCP, whereas in VPS13B KO cells mitochondrial GABARAPL1 was nearly undetectable at baseline and failed to increase with CCCP; mitochondrial LC3B was also reduced, though less profoundly. By contrast, EGFP-Parkin and PINK1 accumulated on mitochondria in KO cells even without CCCP, consistent with damaged mitochondria that recruit the PINK1/Parkin machinery but fail to engage downstream ATG8 steps (Fig. 3C, D). To examine flux, we profiled mammalian ATG8 (mATG8) family members (GABARAP,

GABARAPL2, LC3A, LC3C) in presence and absence of bafilomycin A1 (Supplementary Fig. 2): GABARAPL1-II—a key effector in PINK1/Parkin-mediated mitophagy—was reduced in KO cells and did not increase with CCCP (Fig. 3C, D), and its BafA1-sensitive turnover was blunted (Supplementary Fig. 2). In contrast, LC3A/B-II increased with CCCP in KO similarly to WT, and GABARAPL2 levels were lowered with only a mild flux decrease; p62/SQSTM1 levels and flux were also reduced in KO (Fig. 3C, D). Together with the MitoQC data showing reduced mitolysosome formation in KO and rescue of mitolysosome number by full-length VPS13B, these findings indicate that VPS13B could enable the GABARAP or GABARAPL1-dependent arm of PINK1/Parkin-mediated mitophagy. Notably, the CCCP-induced mitochondrial recruitment of VPS13B in WT places VPS13B at the site of damage, where it likely couples Parkin/PINK1 activation to productive mATG8 (GABARAP and GABARAPL1) engagement, thereby maintaining mitochondrial quality control.

VPS13B is recruited to Mfn2-positive mitochondria via its MLD, and this recruitment is enhanced by mitochondrial stress

Next, to test whether endogenous VPS13B is dynamically recruited to Mfn2-positive mitochondria(used as a marker for ER-mitochondria contact sites) under cellular stress, we quantified VPS13B-Mfn2 PLA signals after applying mitochondrial depolarization (CCCP), oxidative stress (Sodium Arsenite, S.A.), and ER stress (Thapsigargin, T.G.) (Fig. 3E, F). Notably, CCCP elicited a significant increase in VPS13B-Mfn2 PLA puncta in WT cells, indicating stress-induced engagement of VPS13B at Mfn2-positive mitochondria (Fig. 3E, F). This finding is concordant with our biochemical fractionation data showing CCCP-dependent enrichment of VPS13B in the crude mitochondrial fraction (Fig. 3C, D), together supporting a model in which mitochondrial stress promotes VPS13B recruitment to Mfn2-positive mitochondria interfaces. Collectively, these results demonstrate that mitochondrial stress promotes VPS13B recruitment to Mfn2-positive mitochondria contact sites, consistent with its CCCP-dependent enrichment in the mitochondrial fraction.

VPS13B recruits PI4P-positive Golgi vesicles to mitochondrial fission sites via its MLD

Having established that VPS13B-deficient cells exhibit hyperfused mitochondria with membrane depolarization and reduced outer-membrane dynamics, and that VPS13B is recruited via its C-terminal MLD to Mfn2-positive mitochondria, particularly under mitochondrial stress, we next investigated the functional role of VPS13B at these mitochondrial sites.

Recent work implicates PI4P-containing Golgi-derived vesicles in mitochondrial fission[39], yet how these vesicles are coupled to the fission machinery remains poorly defined. We next examined mitochondrial network architecture under PI4P depletion in our system, to test whether the previously reported fission defects upon phosphatidylinositol 4-kinase beta (PI4KB) knockdown were reproducible under our conditions. We acutely depleted PI4P by siRNA-mediated knockdown of PI4KB, validated by reduced PI4KB protein levels on Western blot (Supplementary Fig. 3a, b). To visualize PI4P dynamics in cells, we used GFP tagged PH domain of the oxysterol-binding protein-related protein 9 (GFP-ORP9-PH) domain, which binds to specifically to PI4P[40]. PI4P depletion led to decreased mean GFP-ORP9-PH intensity normalized to cellular area (Supplementary Fig. 3c, d), along with increases in accumulation of hyperfused mitochondrial networks (Supplementary Fig. 3c, e). These findings indicate a more reticulated and branched mitochondrial network with increased terminal ends—a signature of stalled or aborted fission that corroborates prior studies and confirms that PI4P depletion alone is sufficient to impair mitochondrial fission under our conditions as well as network architecture under PI4P depletion condition. Thus, when PI4P is depleted, mitochondria become more reticulated with greater branching and more terminal ends—a signature of stalled or aborted fission[39].

Given VPS13B's localization and link to mitochondrial function, we hypothesized that VPS13B mediates this coupling for PI4P transport. To test this hypothesis, we quantified mitochondrial fission by live-cell imaging of MitoTracker-stained mitochondria with event-based scoring in WT and VPS13B KO cells: the normalized fission rate was significantly reduced in KO relative to WT, indicating a VPS13B-dependent deficit in mitochondrial fission (Fig. 4A, B).

To test whether the fission defect reflects impaired delivery of Golgi derived PI4P-positive vesicles to fission sites, we performed three-color live-cell imaging in WT and KO cells expressing EGFP-TGN46 (Golgi marker), BFP-ORP9-PH (PI4P reporter), and MitoTracker, and quantified—on an event basis—the fraction of bona fide fission events exhibiting (i) PI4P contact at mitochondria, (ii) TGN46 contact, and (iii) dual PI4P-TGN46 contact. All three metrics were significantly reduced in KO vs WT, indicating that VPS13B is required for recruitment/retention of PI4P-positive TGN vesicles at mitochondrial fission sites (Fig. 4B–E; Supplementary Movie 1, 2).

To determine whether VPS13B is sufficient to drive PI4P-vesicle delivery to fission sites, we imaged VPS13B KO cells co-expressing VPS13B-EGFP (FL or ΔMLD), BFP-ORP9-PH, and MitoTracker (Fig. 4F, G). Re-expression of VPS13B-FL rescued the normalized fission rate to WT-like levels, whereas VPS13B-ΔMLD failed to rescue (Fig. 4g, h; Supplementary Movie 3–6). Consistent with a direct role at fission, VPS13B-FL localized at a substantial fraction of fission events (VPS13B contact at mitochondrial fission site, %) comparable to WT, while ΔMLD showed no localization (Fig. 4H). Likewise, PI4P contact at mitochondrial fission site (%) was rare in KO, restored by VPS13B-FL, and not rescued by ΔMLD (Fig. 4I). Importantly, co-occurrence of PI4P and VPS13B at the same fission site was readily detected in WT and KO + VPS13B-FL but absent with ΔMLD (Fig. 4J). Event tracking further revealed that VPS13B and PI4P signals converged at ~30.1% of fission events (WT cells VPS13B contact at mitochondrial fission site, Fig. 4H; Supplementary Movie 3), and in ~93.8% of those convergent events the ORP9-PH-positive vesicle arrived with VPS13B and reached mitochondria prior to fission (WT cells PI4P-VPS13B contact at mitochondrial fission site, Fig. 4J; Supplementary Movie 3), consistent with targeted delivery of PI4P-positive vesicles to maturing fission sites. In KO cells, overexpression of VPS13B-ΔMLD failed to restore fission and instead further suppressed residual fission activity compared to VPS13B-FL, suggesting that the mutant exerts a nonfunctional or inhibitory effect (Fig. 4F–J; Supplementary Movies 5–6).

Finally, to establish biochemical competence for PI4P recognition, we purified a GST-tagged VPS13B PH domain in *E. coli* expression system and performed a PIP-strip assay. The VPS13B PH domain bound PI4P and, to varying degrees, PI3P, PI5P, PI(3,4)P_2, PI(3,5)P_2, PI(4,5)P_2, and PI(3,4,5)P_3, whereas GST alone showed no detectable binding (Supplementary Fig. 3f–h). Together, these quantitative imaging, rescue, and biochemical data demonstrate that VPS13B, through its MLD, recruits PI4P-containing Golgi vesicles to mitochondrial fission sites to promote efficient fission, providing a mechanistic basis for the reduced fission and hyperfusion observed in VPS13B-deficient cells.

PI4P-VPS13B acts downstream of Drp1 to drive late-stage mitochondrial fission

Given that VPS13B recruits PI4P-positive Golgi vesicles to mitochondrial fission sites, we next examined how PI4P itself contributes to mitochondrial fission and interfaces with VPS13B function. To this end, we acutely depleted PI4P using siPI4KB. Event-based live imaging of MitoTracker-labeled mitochondria revealed that PI4P depletion significantly lowered both the number of fission events and the normalized fission rate, thereby phenocopying the VPS13B KO defect (Supplementary Fig. 4a–c). Importantly, the fraction of Drp1-positive fission events (BFP-Drp1) was unchanged in PI4P depletion condition

https://doi.org/10.1038/s41467-025-67445-6

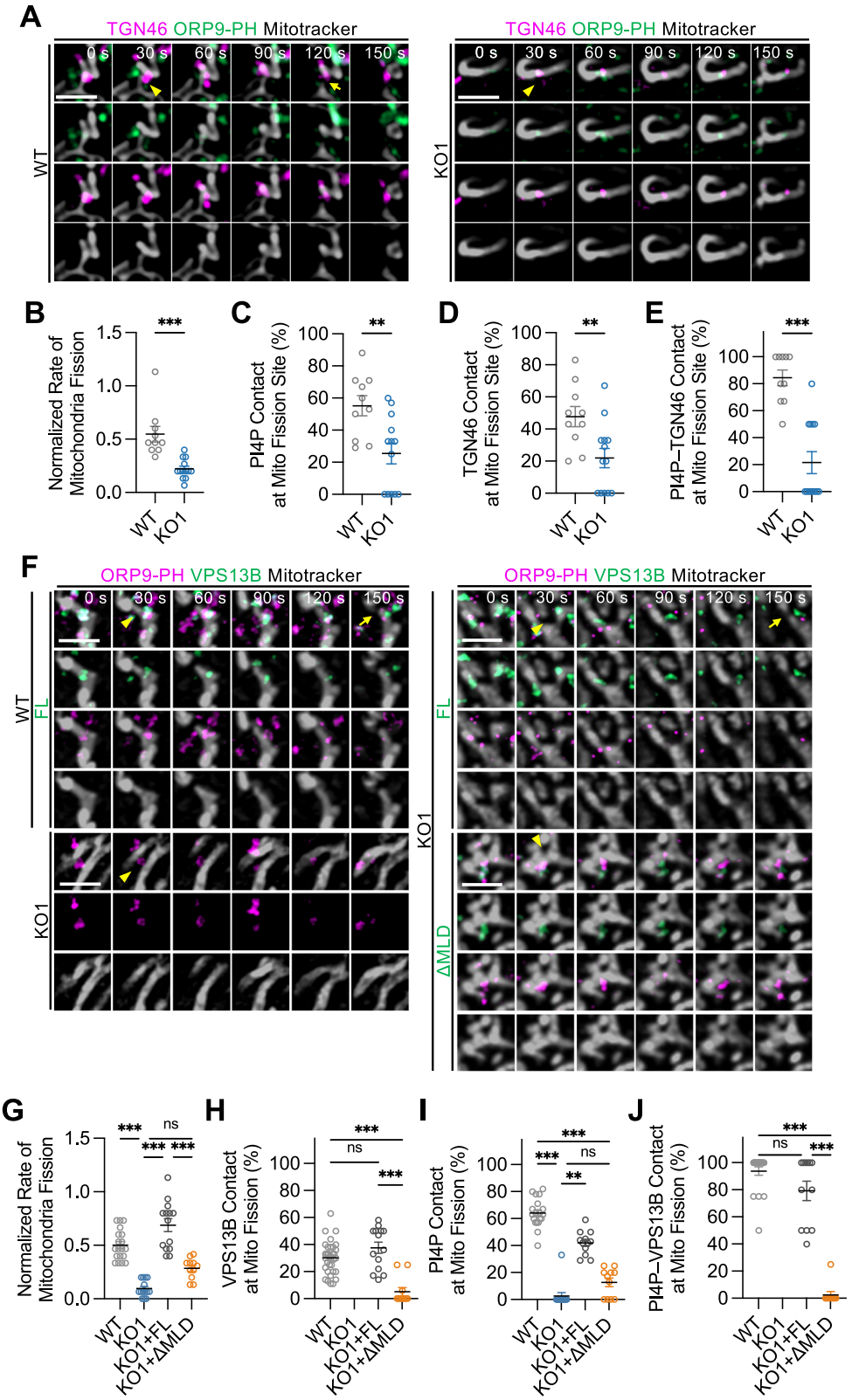

(Supplementary Fig. 4d), and neither the MitoTracker-Drp1 colocalization (%) nor the number of Drp1 puncta per cell differed from control (Supplementary Fig. 4e–g), indicating that Drp1 recruitment and puncta assembly are preserved, while completion of mitochondrial fission is impaired. Immunoblotting further supported this interpretation: total Drp1 protein decreased upon PI4P depletion, with a slight increase in Mfn2 levels noted, while the ratios of phospho-Drp1 (S616, activating) and phospho-Drp1 (S637, inhibitory) to total Drp1 remained unchanged, arguing against a shift in Drp1 activation state as the primary driver of the defect (Supplementary Fig. 4h–l). Consistently, VPS13B KO cells also exhibited decreased total Drp1 levels, and combining PI4P depletion with VPS13B loss produced an additive reduction in Drp1 abundance (Supplementary Fig. 4i). Nonetheless, the Drp1-positive fission fraction, Drp1-mitochondria colocalization, and

Fig. 4 | VPS13B contacts mitochondrial fission sites via its MLD domain in a PI4P-dependent manner. A Live cell imaging of WT and KO cells transfected with GFP-ORP9-PH and BFP-TGN46, and stained with MitoTracker. Arrowheads point to mitochondria contact site, arrow point to mitochondria fission site. Data are representative of 3 independent experiments. Scale bars, 2 μm. **B**–**E** Quantification of mitochondrial fission events **B**, mitochondrial fission events in contact with PI4P **C**, TGN46 **D**, and both PI4P and TGN46 **E**. Analysis via two-tailed Mann-Whitney test. **B** ***$p < 0.001$, **C** **$p = 0.01$, **D** **$p = 0.007$, **E** ***$p < 0.001$. WT; $n = 10$, KO; $n = 13$ cells. All data are obtained from 3 independent experiments. **F** Live cell imaging of WT and KO cells transfected with BFP-ORP9-PH, EGFP-VPS13B FL or ΔMLD and stained with MitoTracker. Arrowheads point to mitochondria contact and fission site, arrow point to mitochondria fission site. Scale bars, 2 μm. (G-J) Quantification of mitochondrial fission events **G**, mitochondrial fission events in contact with VPS13B **H**, PI4P **I**, and both VPS13B and PI4P **J**. Analysis via Kruskal-Wallis with Dunn's test. **G** ***$p < 0.001$, n.s. = not significant. **H** ***$p < 0.001$, **I** ***$p < 0.001$, **$p = 0.004$, **J** ***$p < 0.001$, n.s. = not significant. WT; $n = 19$, KO1; $n = 13$, KO1 + FL; $n = 12$, KO1 + ΔMLD; $n = 11$ cells. WT; $n = 20$, KO1 + FL; $n = 12$, KO1 + ΔMLD; $n = 10$ cells. All data are obtained from 3 independent experiments. Data are presented as mean ± SEM.

puncta number remained stable (Supplementary Fig. 4d, f, g), reinforcing the conclusion that VPS13B and PI4P regulate the fission completion step rather than Drp1 recruitment or activation. Together, these data place PI4P—and thus VPS13B-mediated PI4P vesicle delivery—downstream of or parallel to Drp1 recruitment, acting at a late, lipid-dependent step required for productive mitochondrial fission. In this model, Drp1 is properly recruited and assembled, but in the absence of adequate PI4P-dependent lipid supply or membrane organization, the mitochondrial fission fails to progress to membrane severing despite an intact phosphorylation balance.

To determine whether VPS13B localizes to mitochondrial fission sites and to assess the functional requirement of its MLD, we performed three-color live-cell imaging (MitoTracker, VPS13B-EGFP, and BFP-Drp1) and quantified bona fide fission events. In WT cells, VPS13B and Drp1 co-localized at mitochondria (Fig. 5A, B). In VPS13B-KO cells, re-expression of full-length VPS13B (VPS13B-FL) restored multiple parameters: (i) the normalized mitochondrial fission rate was restored to ~0.51 (Fig. 5C, D), (ii) Drp1 contact at fission sites was detected in ~77.2% of events (Fig. 5C, E), (iii) VPS13B contact at fission sites was observed in ~51.3% (Fig. 5C, F), and (iv) dual Drp1-VPS13B contact at fission sites occurred in ~68.1% of events (Fig. 5C, G; Supplementary Movie 7). By contrast, VPS13B-ΔMLD failed to restore any of these parameters, all of which remained significantly reduced relative to KO + VPS13B-FL (Fig. 5C–G; Supplementary Movie 8). These findings position VPS13B at Drp1-positive mitochondrial fission sites and demonstrate that the MLD is essential for its engagement with, and PI4P-dependent support of, the fission machinery.

CS patient derived iPSC-induced neurons recapitulate VPS13B-linked mitochondrial dysfunction and mitophagy defects

Cohen syndrome (CS) is a rare, autosomal-recessive neurodevelopmental disorder caused by biallelic pathogenic variants in *VPS13B* (COH1)[11,14,15,41–43]. Clinically, CS features developmental delay/intellectual disability, postnatal microcephaly, early hypotonia, progressive retinochoroidal dystrophy with high myopia, neutropenia, truncal obesity, joint laxity, and a characteristic facial gestalt[42,43]. Most reported *VPS13B* variants are loss-of-function (e.g., nonsense/frameshift or large deletions) predicted to abolish protein function[11,43].

To assess clinical relevance, we analyzed iPSC-induced neurons from CS patients harboring VPS13B loss-of-function variants (*c.1239 T > G* and *c.10333 G > A*), comparing them with three healthy control lines[21,29]. As reported in these prior studies, the VPS13B Compound Heterozygote variants in these CS lines lead to an approximately ~50% reduction in VPS13B mRNA levels in patient-derived neural cells, consistent with a partial loss-of-function effect. Consistent with our VPS13B KO model, MitoTracker imaging revealed accumulation of hyperfused mitochondrial networks in CS neurons (Fig. 6A, B). Mitochondrial membrane potential (ΔΨm), quantified as TMRM intensity normalized to MitoTracker-positive area, was significantly reduced in CS neurons relative to controls (Fig. 6C, D). At the level of fission/fusion regulators, PINK1 puncta were increased (Fig. 6E, F) and Drp1 puncta were decreased (Fig. 6G, H), indicating persistent mitochondrial damage signals and suggesting impaired mitophagy progression. A directional increase in Mfn2 puncta was also observed (Supplementary Fig. 5a, b), but we do not over-interpret this finding here, as it may reflect multiple processes, including mitochondrial fusion and/or ER–mitochondria contact formation. Accordingly, while our data primarily indicate an impairment in mitochondrial fission, a potential contribution of VPS13B to fusion or contact-site remodeling cannot be excluded.

Taken together, CS patient neurons recapitulate the core VPS13B-linked phenotypes—hyperfused networks, reduced ΔΨm, decreased Drp1, and elevated PINK1—supporting a shared mechanism in which VPS13B dysfunction compromises mitochondrial dynamics and quality control.

As these findings are based on two CS lines and may represent a subset of CS presentations, larger cohorts and isogenic correction or rescue studies will be needed to generalize; nonetheless, the convergence with VPS13B-deficient models suggests a clinically relevant pathway and highlights VPS13B-dependent lipid and vesicle trafficking as a potential therapeutic entry point.

Discussion

Our results support a model in which VPS13B contributes to mitochondrial network maintenance and quality control by localizing, via its C-terminal MLD, to Mfn2-positive mitochondria interfaces and engaging PI4P-positive Golgi vesicles, whose precise identity and cargo remain to be determined, to promote late-stage fission. In VPS13B KO cells, we observe hyperfused networks, reduced ΔΨm normalized to mitochondrial mass, impaired mitochondrial membrane mobility and membrane dynamics, decreased fission frequency, and blunted PINK1/Parkin-mediated mitophagy—each rescued by full-length VPS13B but not by ΔMLD. Event-based imaging shows VPS13B accumulation with Drp1 at fission sites and restored PI4P-vesicle contacts, while PI4KB knockdown lowers fission without altering Drp1 recruitment or phosphorylation, placing PI4P-VPS13B action downstream/parallel to Drp1 assembly. Consistent with clinical relevance, CS iPSC-induced neurons display hyperfused networks and reduced ΔΨm, aligning with the KO/rescue phenotypes. Together, these findings define a VPS13B-dependent, PI4P-sensitive pathway that facilitates efficient mitochondrial fission and mitophagy in our systems and offers testable hypotheses for therapeutic modulation.

Previous studies have reported that VPS13 family members localize to membrane contact sites between organelles, facilitating lipid transport essential for maintaining organelle identity and function[4,6,7,26,33]. Notably, VPS13A and VPS13C have been linked to mitochondrial-ER contacts, which are critical for lipid exchange and calcium homeostasis[7,25,44]. Domain mapping and proximity ligation assays indicate that VPS13B's mitochondrial engagement is mediated by its C-terminal MAM localization domain (MLD): deleting the MLD prevents VPS13B accumulation at Mfn2-positive mitochondria contacts and fails to rescue the hyperfused morphology in KO cells, whereas C-terminal DHL-PH/MLD fragments are sufficient for mitochondrial targeting (Fig. 1G–J). This parallels findings for VPS13A, in which the DHL-PH domain mediates ER-mitochondria contact[7]. Building on this framework, our data place VPS13B—via its C-terminal MLD—at Mfn2-positive mitochondria interfaces, where it facilitates the

https://doi.org/10.1038/s41467-025-67445-6

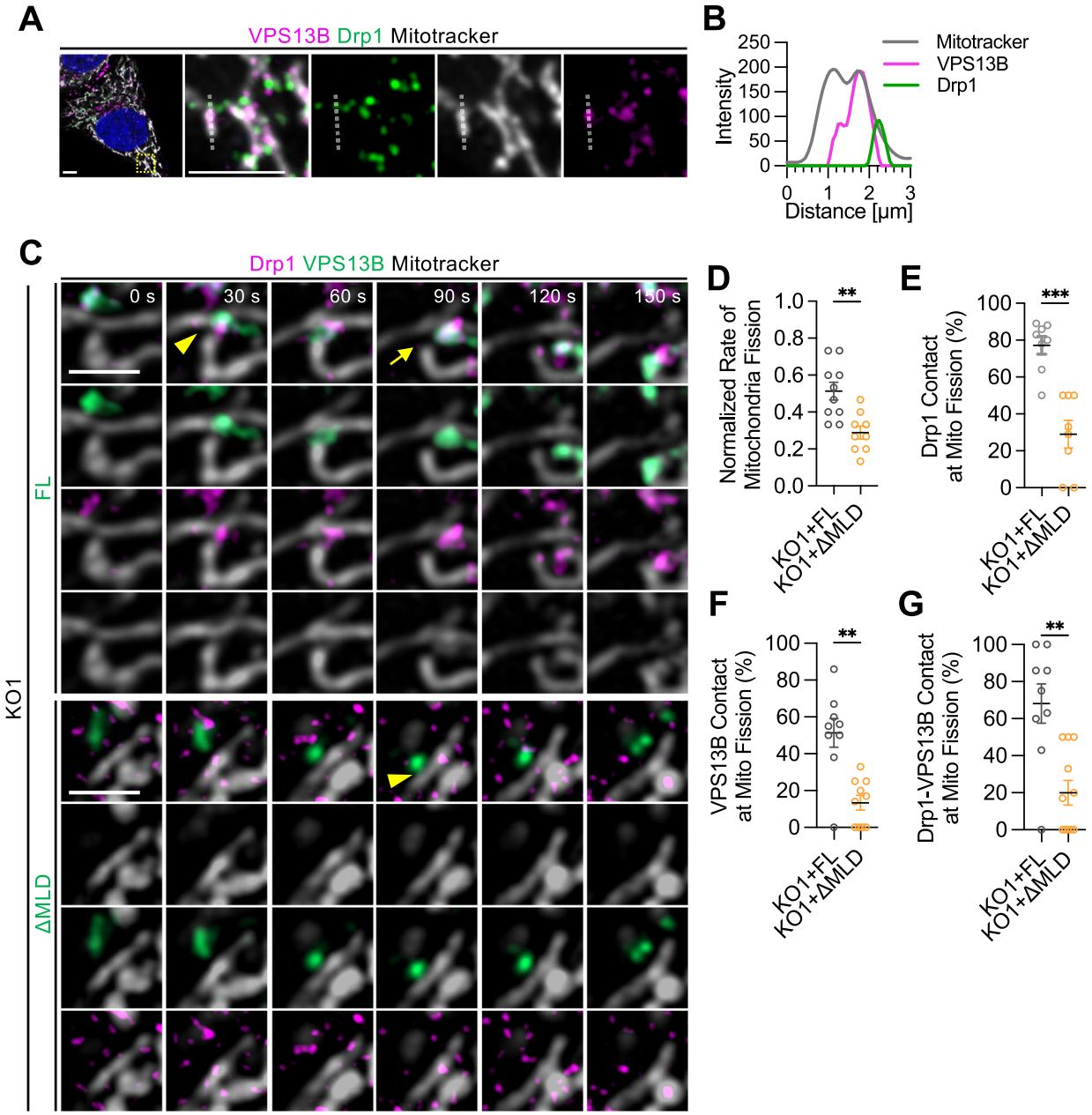

Fig. 5 | VPS13B contacts mitochondrial fission sites with Drp1. A Confocal images of WT cells transfected with EGFP-Drp1, stained with VPS13B antibodies and Mitotracker. **B** Line scan analysis showing relative fluorescence intensity from each labeled protein (Green line: Drp1, Gray line: Mitotracker, Magenta line: VPS13B). Scale bars, 5 μm. **C** Live cell imaging of KO cells transfected with BFP-Drp1, VPS13B-FL-EGFP or VPS13B-ΔMLD-EGFP and stained with MitoTracker. Arrowheads point to the mitochondria contact site, and arrows point to the mitochondria fission site. Scale bars, 2 μm. **D**–**G** Quantification of mitochondria fission events in contact **D**, mitochondrial fission events in contact with Drp1 **E**, VPS13B **F**, and both Drp1 and VPS13B **G**. Analysis via two-tailed Mann-Whitney test. **D** $^{**}p = 0.002$, **E** $^{***}p < 0.001$, **F** $^{***}p = 0.001$, **G** $^{**}p = 0.002$, KO1 + FL; $n = 9$, KO1 + ΔMLD; $n = 11$ cells. All data are obtained from 3 independent experiments. Data are presented as mean ± SEM.

recruitment/retention of PI4P-positive, TGN-derived vesicles at Drp1-marked fissions; full-length VPS13B, but not ΔMLD, restores reduced fission rates and relieves hyperfusion in VPS13B KO cells. We also note a modest increase in Mfn2 signal in VPS13B KO cells and CS iPSC-induced neurons; while this leaves open a potential contribution of VPS13B to mitochondrial fusion or contact-site remodeling, the present work focuses on fission mechanisms. Moreover, PI4P depletion (siPI4KB) lowers fission frequency and produces a reticulated network without altering Drp1 recruitment or phosphorylation, positioning the PI4P-VPS13B axis as a late-stage, lipid-dependent facilitator of fission rather than a driver of Drp1 assembly. Thus, rather than asserting direct lipid transfer, our results support a model in which VPS13B coordinates vesicle-mediated PI4P delivery to maturing fission sites[39], enhancing mitochondrial fission efficiency. For instance, the addition of a PI4P-rich vesicle membrane at a Drp1-constricted site may help to actually sever the mitochondrial outer membrane – by providing extra lipid content or inducing curvature – thereby allowing fission to complete. This concept aligns with emerging evidence that lipid signaling plays a vital role in mitochondrial fission[39], and extends the functional repertoire of VPS13 proteins to include Golgi-to-mitochondria PI4P vesicle engagement at sites of fission.

While these data position VPS13B at Mfn2-positive mitochondria contacts and show PI4P dependence for efficient fission, we did not directly tested whether an increase in VPS13B or PI4P supply alone is

https://doi.org/10.1038/s41467-025-67445-6

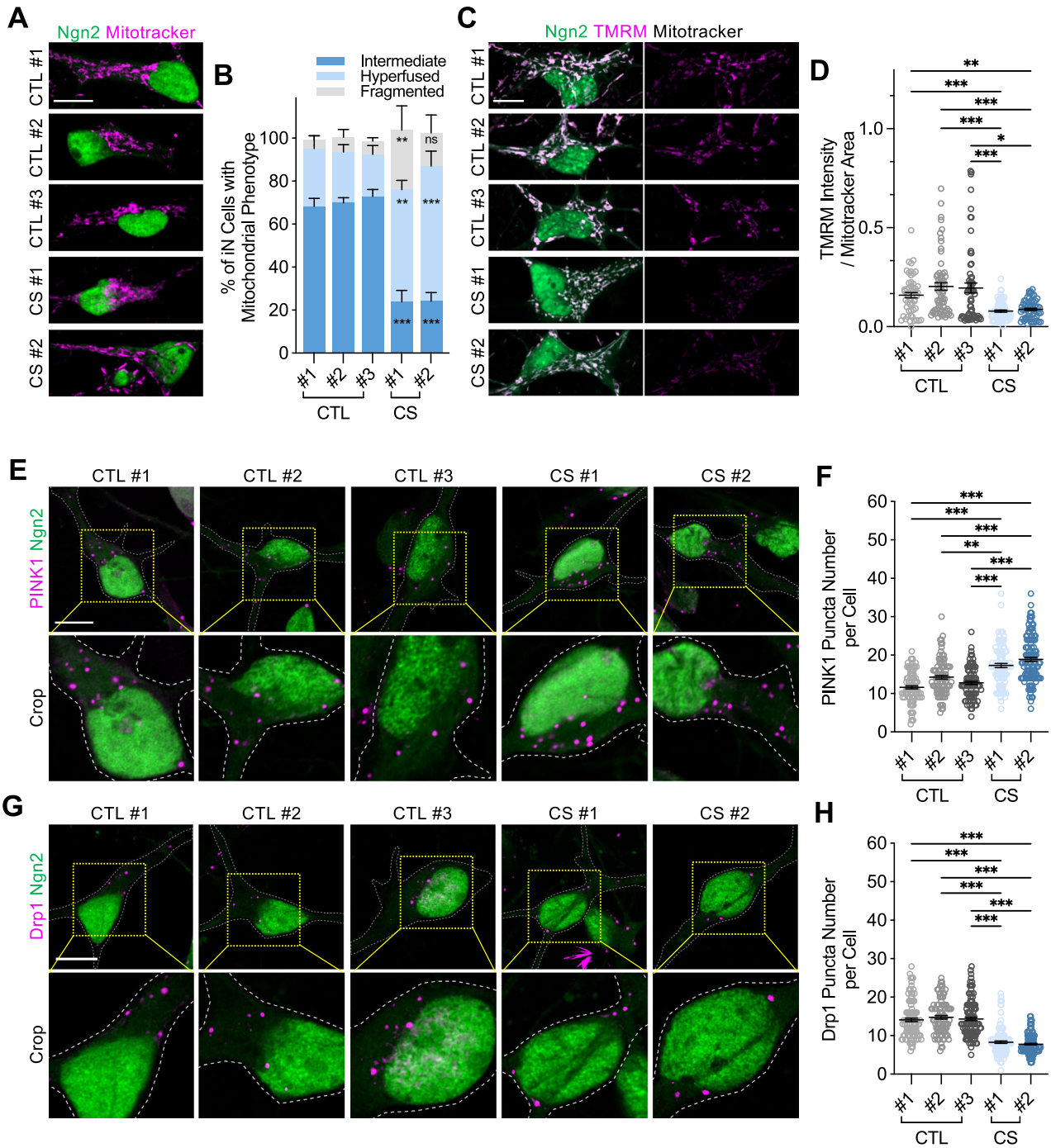

Fig. 6 | Cohen syndrome patient derived iPSC-induced neurons show defective mitochondrial quality control. A Control (CTL) and Cohen syndrome patient (CS) iN cells induced via EGFP-Ngn2 and rtTA, stained with MitoTracker. Scale bars, 10 μm. **B** Quantification of mitochondrial morphology. Analysis via Kruskal-Wallis with Dunn's test. Fragmented: $^{**}p > 0.99$, Intermediate: $^{***}p < 0.001$, Hyperfused: $^{**}p = 0.005$, $^{***}p < 0.001$, n.s. = not significant. CTL #1; $n = 92$, CTL #2; $n = 107$, CTL #3; $n = 143$, CS #1; $n = 124$, CS #2; $n = 164$ cells. All data are obtained from 4 independent experiments. **C** CTL and CS iN cells stained with TMRM and MitoTracker Deep Red. Scale bars, 10 μm. **D** Quantification of TMRM intensity normalized to MitoTracker area. Analysis via Kruskal-Wallis with Dunn's test. $^{***}p < 0.001$, $^{**}p = 0.001$, $^{*}p = 0.01$. CTL #1; $n = 54$, CTL #2; $n = 66$, CTL #3; $n = 66$, CS #1; $n = 74$, CS #2; $n = 63$ cells from 4 independent experiments. **E** CTL and CS iN cells immunostained for PINK1. Scale bars, 10 μm. **F** Quantification of PINK1 puncta. Analysis via Kruskal-Wallis with Dunn's test. $^{***}p < 0.001$, $^{**}p = 0.001$, n.s. = not significant. CTL #1; $n = 105$, CTL #2; $n = 92$, CTL #3; $n = 92$, CS #1; $n = 102$, CS #2; $n = 130$ cells. All data are obtained from 6 independent experiments. **G** CTL and CS iN cells immunostained for Drp1. **H** Quantification of Drp1 puncta. Analysis via Kruskal-Wallis with Dunn's test. $^{***}p < 0.001$, n.s. = not significant. CTL #1; $n = 107$, CTL #2; $n = 98$, CTL #3; $n = 116$, CS #1; $n = 133$, CS #2; $n = 160$ cells. All data are obtained from 6 independent experiments. Data are presented as mean ± SEM.

sufficient to drive mitochondrial fission, and the molecular linkage to the fission machinery remains incompletely defined. For example, it is not yet clear whether VPS13B directly facilitates the membrane fission step or if it acts through interactions with Drp1's cofactors (Mff, MiD49, MiD51, or Fis1) at fission sites. Future studies combining live-cell super-resolution imaging, interaction mapping, and minimal reconstitution assays are needed to determine whether VPS13B stabilizes Drp1 assemblies, organizes PI4P-rich membranes, and/or recruits

accessory factors required for late-stage mitochondrial fission. Furthermore, recent evidence suggests that enhancing PI4P synthesis via PI4KB overexpression can promote mitochondrial fission and fragmentation[45]. Consistent with this, our findings suggest that local PI4P accumulation is a rate-limiting step for fission. Future studies investigating whether PI4P supplementation or PI4KB overexpression can rescue the fission defects in VPS13B-deficient cells will be crucial to definitively establish the VPS13B–PI4P axis as a rate-limiting facilitator that creates a lipid microenvironment permissive for membrane constriction[45]. Moreover, we did not directly test whether augmenting PI4P availability or VPS13B expression can actively promote mitochondrial fission, thus, the sufficiency of the PI4P–VPS13B axis in driving fission remains to be determined. Future studies combining live-cell super-resolution imaging, interaction mapping, and minimal reconstitution assays are needed to determine whether VPS13B stabilizes Drp1 assemblies, organizes PI4P-rich membranes, and/or recruits accessory factors required for late-stage mitochondrial fission.

In addition to effects on mitochondrial dynamics, our data indicate that VPS13B contributes to mitochondrial quality control by selectively supporting PINK1/Parkin-mediated mitophagy. In VPS13B KO cells, mitolysosome formation was reduced, PINK1 and Parkin accumulated on mitochondria even at baseline, and GABARAPL1 was nearly absent from the mitochondrial fraction and failed to increase upon CCCP; re-expression of full-length VPS13B restored mitolysosome counts toward WT, and in WT cells VPS13B was enriched in the mitochondrial fraction after CCCP, placing it at sites of damage. Notably, under CCCP-induced mitochondrial stress, endogenous VPS13B localizes to Mfn2-positive mitochondria contact sites, highlighting its dynamic recruitment to damaged organelles and underscoring a direct role in coordinating lipid-containing vesicle exchange and fission–mitophagy coupling at these interfaces.

By contrast, LC3A/B-II levels were accumulated in KO cells compared to WT upon CCCP treatment. This enhanced accumulation argues against a failure in general autophagic induction and may instead reflect a compensatory response or stalled turnover due to the selective deficit in the GABARAPL1-dependent arm of mitophagy. This selective effect mirrors recent reports that mitophagy can be regulated by distinct autophagic pathways depending on the type and severity of mitochondrial damage[46–48]. Mitochondrial quality control is multifaceted—encompassing fusion–fission, mitophagy, and biogenesis—and, while our study focused on mitophagy, whether VPS13B also influences mitochondrial biogenesis or other turnover pathways remains to be determined.

Patient-derived iPSC induced neurons from individuals with CS recapitulate the mitochondrial abnormalities seen in VPS13B KO cells—reduced membrane potential, hyperfused networks, and impaired mitophagy—supporting clinical relevance for a subset of CS cases, particularly those harboring VPS13B variants that reduce protein abundance and/or are predicted loss-of-function[11,21,43]. Given the genetic and phenotypic heterogeneity of CS and the limited number of lines examined, we do not generalize these findings to all VPS13B genotypes; larger cohorts and isogenic correction studies will be required. Furthermore, it remains to be determined whether other VPS13 paralogs (VPS13A/C/D) are misregulated or provide compensatory functions in these patient-derived lines, which could contribute to the phenotypic heterogeneity observed in Cohen syndrome. Nevertheless, if this VPS13B-linked, PI4P-dependent fission/mitophagy pathway operates in even a subset of patients, it offers a mechanistic foothold for hypothesis-driven studies and points to mitochondrial dynamics and quality control as tractable therapeutic entry points. More broadly, because mitochondrial dysfunction is a common feature across neurodegenerative conditions, delineating VPS13B's contribution to these processes may yield insights that extend beyond CS.

Altogether, our study identifies VPS13B as a key mediator of mitochondrial fission and mitophagy, functioning through a PI4P-dependent vesicle engagement mechanism at Mfn2-positive-mitochondria contact sites. By coordinating the recruitment of Golgi-derived vesicles to Drp1-marked fissions, VPS13B ensures efficient mitochondrial fission and quality control via selective mitophagy. These findings extend the functional repertoire of the VPS13 protein family and provide mechanistic insight into how inter-organelle lipid trafficking can dynamically regulate mitochondrial integrity. Therefore, this work not only defines a PI4P–VPS13B axis critical for maintaining mitochondrial homeostasis but also highlights its potential pathophysiological relevance in Cohen syndrome and related disorders involving VPS13B dysfunction.

Methods

All experiments were performed in accordance with relevant ethical regulations and were approved by the Institutional Review Board and the Institutional Animal Care and Use Committee of Hannam University.

Cell culture and transfections

HeLa and LX293T cells were obtained from the American Type Culture Collection (ATCC, Manassas, VA, USA) and Clontech (Takara, Shiga, Japan). The cells were cultured in Dulbecco's Modified Eagle's Medium (DMEM; Corning, Corning, NY, USA) with high glucose, supplemented with 10% fetal bovine serum (FBS; Corning) and 100 U/mL penicillin-streptomycin (GIBCO, Billings, MT, USA), and maintained at 37 °C with 5% CO_2. All cell lines were confirmed to be mycoplasma-free using the EZ-PCR Mycoplasma Detection Kit (Biological Industries, Cromwell, CT, USA; Cat# 20-700-20).

For transfections, cells were seeded and transfected with either Lipofectamine 2000 or Lipofectamine 3000 (Invitrogen, Waltham, MA, USA) according to the manufacturer's protocols, and incubated for 24 h. Lentiviral packaging was performed in LX293T cells using the CalPhos transfection system (Clontech), following the manufacturer's instructions. Briefly, the packaging plasmids psPAX2 (Addgene, Watertown, MA, USA; #12260), pMD2.G (Addgene; #12259), and the construct of interest were transfected at a 4:1:5 ratio. Afterward, lentiviral supernatants were collected 48 h post-transfection, followed by a second collection 72 h after media replacement.

For transduction, EGFP-Parkin and Myc-Parkin lentiviruses were introduced into HeLa cells in the presence of 10 μg/mL polybrene (Hexadimethrine bromide; Sigma-Aldrich, St. Louis, MO, USA). After 48 h, cells were selected with 1 μg/mL puromycin for an additional 48 h and subsequently sorted by FACS to optimize GFP expression.

iPSC culture and glutamatergic neuronal induction

All research involving human stem cells was conducted in accordance with all relevant guidelines and regulations and was approved by the Institutional Review Board of Hannam University (IRB No. 2024-021). Informed consent was obtained from all donors for the use of human cells in this study. Patient-derived and control induced pluripotent stem cells (iPSCs) were maintained following established protocols[21,29,49]. Briefly, iPSC lines were cultured in an embryonic stem cell (ESC) medium containing 20% knockout serum (Gibco; 10828-028), beta-mercaptoethanol (Gibco; 21985-023), 1×GlutaMAX (Gibco; 3500-061), 1×MEM-NEAA (Gibco; 1140-050), penicillin/streptomycin (Gibco; 15140-122), and DMEM-F12 (Gibco; 11320-033). Next, iPSC-like colonies were picked after 1 month and reseeded onto new feeder cells. The iPSC culture system was subsequently transitioned from a mouse embryonic fibroblast (MEF) feeder-dependent system to a feeder-free system using Essential 8 Medium (Gibco; A1517001) between passages 5 and 7. For glutamatergic neuronal induction, a modified neurogenin2 (Ngn2)-mediated rapid neural induction protocol was employed as described in previous studies[50].

Plasmids and reagents

The following plasmids were used: pGEX[51], pCMV-BFP-KDEL (Addgene; #49150), pEGFP-GalT, pEGFP-LAMP1, pEGFP-Rab5, pEGFP-Rab7,

pEGFP-Rab9, pEGFP-Sec61, mCherry-Sec61, pcDNA3.1-mRFP-TOM20 and pPBbsr-AcGFP1-ORP9-PH(Addgene; #214270). The following plasmids were constructed for this study. Primer sequences are detailed in Supplementary Table 1. pGEX-PH domain, pcDNA3.1-mCherry-EGFP-FIS1 (MTS) (MitoQC), pEGFP-Drp1, pCMV-BFP-Drp1, pCMV-BFP-ORP9-PH, pEGFP-N3-VPS13B, pEGFP-N3-VPS13B-ΔMLD, pEGFP-N3-DHL-PH (VPS13B), pEGFP-N3-MLD (VPS13B), pCMV7.1-3xFlag-DHL-PH (VPS13B), pCMV7.1-3xFlag-MLD (VPS13B), The sequences for FIS1 (MTS), Drp1, and VPS13B, VPS13B MLD were amplified from a WT HeLa cDNA library.

Reagents were obtained as follows:Image-iT™ TMRM Reagent (I34361) and MitoTracker™ Red CMXRos (M7512) from Invitrogen; MitoTracker ® Deep Red FM (#8778) from CST; Bafilomycin A1 (sc-201550A) from Santa Cruz (Dallas, TX, USA); and, Brefeldin A (B7651), and CCCP (C2759) from Sigma-Aldrich.

Immunofluorescence

Cells were plated on glass coverslips and grown for 24 hours before drug treatment. After treatment, the cells were fixed in 4% paraformaldehyde (PFA) in PBS at room temperature (RT) for 15 minutes. The cells were then blocked with 3% BSA in PBS at RT for 30 minutes, followed by three washes with PBS. Next, the cells were incubated overnight at 4 °C in 3% BSA in PBS with the primary antibodies. After three PBS washes, the cells were stained with the appropriate secondary antibodies (Alexa or DyLight) for 2 hours at RT in PBS. Following three additional washes with PBS, coverslips were mounted onto slides with DAPI-containing mounting solution (VectorLabs, Newark, CA, USA) or DAKO Fluorescence Mounting Medium (DAKO, Carpinteria, CA, USA).

Antibodies

Primary antibodies were obtained from the following sources: VPS13B (NBP2-55104), PINK1 (BC100-494), PINK1 (BC100-494) and Drp1 (NB110-55288, for WB) from Novus Biologicals (Littleton, CO, USA); GM130 (PA1-077) from Thermo Fisher Scientific (Waltham, MA, USA); GST(#2622S), LC3A (4599S), LC3B (2775S), LC3C (14723S), GABARAP (13733S), Phospho-Drp1(Ser616, #3455) and Phospho-Drp1(Ser637, #4867) from Cell Signaling Technology (Danvers, MA, USA); GABARAPL1 (GTX132664) and GABARAPL2 (GTX132666) from GeneTex (Irvine, CA, USA); Mitofusin2 (ab56889), Drp1 (ab56788, for ICC) from Abcam (Cambridge, United Kingdom); GFP (75-131) from Neuromab (Davis, CA, USA); PI4KB(13247-1), TOM20 (11802-1-AP, for WB), and TIM23 (11123-1-AP) from Proteintech (Rosemont, IL, USA); GFP(AE078, for PLA) from Ablconal; and α-tubulin (T5168) and β-actin (A5441) from Sigma-Aldrich.

For Western blotting, primary antibodies were used at a 1:50 − 1:10,000 dilution, while peroxidase-conjugated secondary antibodies were used at a 1:10000 dilution in TBST. Peroxidase-conjugated goat anti-rabbit (111-035-144) and peroxidase-conjugated goat anti-mouse (115-035-174) from Jackson ImmunoResearch Laboratories (West Grove, PA, USA).

For immunocytochemistry, the following secondary antibodies were used: Alexa Fluor 647-conjugated goat anti-rabbit (A21245; Invitrogen), Alexa Fluor 488-conjugated donkey anti-rabbit (711-545-152), DyLight 405-conjugated goat anti-rabbit IgG (111-475-144), DyLight 405-conjugated donkey anti-mouse (715-475-150), and Alexa 594-conjugated donkey anti-rabbit (711-585-152), all obtained from Jackson ImmunoResearch Laboratories.

FRAP assay

FRAP assays were performed using a Zeiss LSM 900 confocal microscope equipped with an incubator stage set at 37 °C and 5% CO_2. HeLa cells transfected with mRFP-TOM20 using Lipofectamine 2000 were photobleached using a 594-nm laser at 100% power for 0.5 seconds. Post-bleach images were acquired at 5-second intervals.

Proximity ligation assays (PLA)

HeLa cells were cultured on coverslips. The 24 h after, cells were fixed with 4% paraformaldehyde for 15 min and permeabilized with 0.01% Triton X-100 for 15 min in Room temperature. PLA was performed using the Duolink detection kit (Sigma) following the manufacturer's instructions. The primary antibodies used were Mfn2(Mouse, 67487-1, Proteintech, 1:400), GFP(Mouse, AE078, Abclonal, 1:200) and VPS13B (Rabbit, NBP2-55104, Novus, 1:200). Images were acquired on a Zeiss LSM900 confocal microscope using a 63× oil-immersion objective.

Live cell imaging

Cells were plated on 35 mm confocal dishes (SPL Life Sciences, Korea) for live cell imaging. Time-series images were performed over 15 frames, with Z-stacks comprising three optical sections using a 63× oil-immersion objective. Z-stacks at 0.33 μm intervals, with a temporal resolution of 30.84 seconds per frame (approximately 0.032 frames per second).

Although the frame rate used in live-cell imaging (~30.8 s per frame) under-samples very rapid mitochondrial dynamics, we restricted our analysis to Drp1-positive events that showed a clear transition from a continuous mitochondrion to two separate mitochondria across consecutive frames. The co-recruitment of the fission marker Drp1 (Fig. 5), therefore, provides an anchor that increases our confidence that we are scoring bona fide fission events under identical imaging conditions across genotypes.

Images were processed using "average projection", "smooth", and then analyzed. For mitochondrial staining, cells were incubated with 200 nM MitoTracker Deep Red FM (M22426; Invitrogen) for 20 minutes at 37 °C in a 5% CO_2 incubator. Mitochondrial membrane potential assays were then performed using Image-iT™ TMRM reagent (I34361; Invitrogen). To image mitochondrial fission events, cells were transfected with VPS13B-EGFP, VPS13B-ΔMLD-EGFP, BFP-ORP9-PH, and BFP-Drp1. Foci that crossed mitochondria 0–30 seconds before fission were counted as positive fission events.

Crude mitochondria fractionation

Mitochondria fractionation was performed using briefly described follow method[52]. HeLa cells were dissociated using trypsin-EDTA, pelleted at 300 × g, and washed with PBS (pH 7.4). The pellets were then resuspended in chilled mitochondria isolation buffer (MIB; 220 mM mannitol, 70 mM sucrose, 10 mM Tris-KOH pH 7.4, and 1 mM EDTA) containing protease inhibitors (Sigma-Aldrich) and homogenized using a pestle and 25 G syringe. The homogenates were then centrifuged at 600 × *g* for 5 minutes at 4 °C. The resulting supernatant was centrifuged again at 7000 × *g* for 10 minutes at 4 °C. Afterward, the pellet was washed twice by resuspension in fresh MIB and centrifuged at 7000 × *g*. Next, the cytosolic (supernatant) and mitochondrial (pellet) fractions were collected. The mitochondrial pellet was then resuspended in 1% SDS radioimmunoprecipitation assay (RIPA) buffer containing protease and phosphatase inhibitors (Sigma). Finally, the protein concentrations in both cytosolic and mitochondrial fractions were quantified using the Pierce BCA Protein Assay Kit (Thermo Fisher) and processed using SDS-PAGE and immunoblotting.

Protein extraction and Western blotting

Cells were lysed in RIPA buffer (20 mM Tris pH 8.0, 150 mM NaCl, 1% SDS, 1% deoxycholic acid, and 1% NP-40) supplemented with complete protease and phosphatase inhibitors. Protein concentrations were determined using the Pierce BCA Protein Assay Kit (Thermo Fisher). Proteins were then separated by SDS-PAGE and transferred onto PVDF membranes (0.2 μm pore size; Millipore, Burlington, MA, USA). Next, the membranes were blocked with 5% non-fat milk or 5% BSA in TBST for 30 minutes at RT, followed by incubation with primary antibodies overnight at 4 °C. After three 10-minute washes in TBST, the membranes were incubated with secondary antibodies. The blots were

developed using Immobilon Western Chemiluminescent HRP Substrate (Millipore) and imaged with a digital ECL machine (UVTECH, Liverpool, UK) and the iBright CL750 (Thermo Fisher).

Transmission electron microscopy

Ultrastructural analysis was performed using transmission electron microscopy (TEM). WT and VPS13B KO HeLa cells were cultured on confocal dishes. Cells were fixed immediately with a solution of 1% glutaraldehyde and 1% paraformaldehyde for 1 h, followed by post fixation in 1% osmium tetroxide for 1 h at 4 °C. Afterward, the samples were stained overnight at 4 °C with 1% uranyl acetate, dehydrated through a graded ethanol series, and embedded in epoxy resin (EMS, Hatfield, PA, USA). Ultrathin sections (65 nm) were then cut using an ultramicrotome (Leica Microsystems, Wetzlar, Germany). Next, the sections were stained with UranyLess for 2 minutes, followed by staining with 3% lead citrate for 1 minute. TEM images were acquired using a Tecnai 20 transmission electron microscope (Thermo Fisher Scientific) operating at 120 kV and equipped with a US1000XP camera.

For quantitative analysis, the outlines of mitochondrial profiles were manually traced from multiple non-overlapping fields for each condition using ImageJ/Fiji software (National Institutes of Health). Quantification was performed on a minimum of 100 mitochondria per condition (WT and KO; $n = 5$) in each of two independent experiments. From the resulting traces, the cross-sectional area and perimeter of each individual mitochondrion were calculated.

Image acquisition and processing

Images were acquired using Zeiss LSM 880 and LSM 900 confocal microscopes equipped with a 63× oil-immersion objective. Subsequently, image analysis was performed using ImageJ Fiji (NIH, Bethesda, MD, USA). For morphological analysis, mitochondrial parameters, including puncta count, area, and perimeter, were quantified using the Particle Analysis tool in ImageJ (Fiji). Following the methodology described previously[39], mitochondria were classified into three distinct categories: “fragmented,” where the majority of mitochondria were short and spherical, Defined as a cell containing 20 or more mitochondrial skeletons with zero branches.; “hyperfused,” Defined as a cell containing at least one mitochondrial skeleton with 50 or more branches.; and “intermediate,” where most mitochondria were tubular but neither extensively interconnected nor spherical, Defined as a cell that did not meet the criteria for either ‘Hyperfused’ or ‘Fragmented’.

Statistics and reproducibility

All statistical analyses were performed using GraphPad Prism10. For bar graphs error bars indicate the mean ± standard error of the mean (SEM) from each independent experiment. All data were tested for normality. When a group did not follow a normal distribution, non-parametric tests, including Mann–Whitney test or Kruskal–Wallis test followed by multiple comparisons test, were performed. In contrast, unpaired two-tailed t-tests or one-way ANOVA followed by multiple comparison tests were applied to data that followed a normal distribution. A p-value of <0.05 was considered statistically significant. All experiments were repeated independently at least three times. No statistical method was used to predetermine sample size. Cell images were selected and analyzed randomly. No data were excluded from the analysis. The investigators were blinded to allocation during experiments and outcome assessment. Details of the statistical tests used, exact n values, and definitions of biological versus technical replicates are provided in the corresponding figure legends.

Reporting summary

Further information on research design is available in the Nature Portfolio Reporting Summary linked to this article.

Data availability

The data supporting the findings of this study are available within the article and its Supplementary Information files. Source data are provided with this paper.

References

1. Park, J. S. et al. Yeast Vps13 promotes mitochondrial function and is localized at membrane contact sites. *Mol Biol Cell* **27**, 2435–2449 (2016).
2. Rzepnikowska, W. et al. Yeast and other lower eukaryotic organisms for studies of Vps13 proteins in health and disease. *Traffic* **18**, 711–719 (2017).
3. Park, J. S. & Neiman, A. M. VPS13 regulates membrane morphogenesis during sporulation in Saccharomyces cerevisiae. *J Cell Sci* **125**, 3004–3011 (2012).
4. De, M. et al. The Vps13p-Cdc31p complex is directly required for TGN late endosome transport and TGN homotypic fusion. *Journal of Cell Biology* **216**, 425–439 (2017).
5. Chen, S. et al. Vps13 is required for the packaging of the ER into autophagosomes during ER-phagy. *Proceedings of the National Academy of Sciences* **117**, 18530–18539 (2020).
6. Suzuki, S. W. et al. A role for Vps13-mediated lipid transfer at the ER–endosome contact site in ESCRT-mediated sorting. *J. Cell Biol.* **223**, (2024).
7. Kumar, N. et al. VPS13A and VPS13C are lipid transport proteins differentially localized at ER contact sites. *Journal of Cell Biology* **217**, 3625–3639 (2018).
8. Lees, J. A. & Reinisch, K. M. Inter-organelle lipid transfer: a channel model for Vps13 and chorein-N motif proteins. *Curr Opin Cell Biol* **65**, 66–71 (2020).
9. Ugur, B. et al. VPS13B is localized at the interface between Golgi cisternae and is a functional partner of FAM177A1. *J. Cell Biol.* **223**, (2024).
10. Anding, A. L. et al. Vps13D Encodes a Ubiquitin-Binding Protein that Is Required for the Regulation of Mitochondrial Size and Clearance. *Current Biology* **28**, 287–295.e6 (2018).
11. Kolehmainen, J. et al. Cohen syndrome is caused by mutations in a novel gene, coh1, encoding a transmembrane protein with a presumed role in vesicle-mediated sorting and intracellular protein transport. *Am. J. Hum. Genet.***72**, 10.1086/375454 (2003).
12. Muñoz-Braceras, S., Calvo, R. & Escalante, R. TipC and the chorea-acanthocytosis protein VPS13A regulate autophagy in Dictyostelium and human HeLa cells. *Autophagy* **11**, 918–927 (2015).
13. García-García, E. et al. VPS13A knockdown impairs corticostriatal synaptic plasticity and locomotor behavior in a new mouse model of chorea-acanthocytosis. *Neurobiol. Dis.* **187**, 10.1016/j.nbd.2023.106292 (2023).
14. Zorn, M., Kühnisch, J., Bachmann, S. & Seifert, W. Disease relevance of rare VPS13B missense variants for neurodevelopmental Cohen syndrome. *Sci. Rep.* **12**, 10.1038/s41598-022-13717-w (2022).
15. Balikova, I. et al. Deletions in the VPS13B (COH1) gene as a cause of Cohen syndrome. *Hum. Mutat.* **30**, 10.1002/humu.21065 (2009).
16. Da Costa, R. et al. Vps13b is required for acrosome biogenesis through functions in Golgi dynamic and membrane trafficking. *Cellular and Molecular Life Sciences* **77**, 511–529 (2020).
17. Seifert, W. et al. Cohen syndrome-associated protein, COH1, is a novel, giant Golgi matrix protein required for Golgi integrity. *Journal of Biological Chemistry* **286**, 37665–37675 (2011).
18. Schröder, L. F. et al. VPS13C regulates phospho-Rab10-mediated lysosomal function in human dopaminergic neurons. *J. Cell Biol.* **223**, 10.1083/jcb.202304042 (2024).
19. Lesage, S. et al. Loss of VPS13C Function in Autosomal-Recessive Parkinsonism Causes Mitochondrial Dysfunction and Increases

PINK1/Parkin-Dependent Mitophagy. *Am J Hum Genet* **98**, 500–513 (2016).
20. Seong, E. et al. Mutations in VPS13D lead to a new recessive ataxia with spasticity and mitochondrial defects. *Ann Neurol* **83**, 1075–1088 (2018).
21. Lee, Y. K. et al. Autophagy pathway upregulation in a human iPSC-derived neuronal model of Cohen syndrome with VPS13B missense mutations. *Mol. Brain* **13**, 10.1186/s13041-020-00611-7 (2020).
22. Seifert, W. et al. Cohen syndrome-associated protein COH1 physically and functionally interacts with the small GTPase RAB6 at the Golgi complex and directs neurite outgrowth. *Journal of Biological Chemistry* **290**, 3349–3358 (2015).
23. Duplomb, L. et al. Cohen syndrome is associated with major glycosylation defects. *Hum Mol Genet* **23**, 2391–2399 (2014).
24. Koike, S. & Jahn, R. SNAREs define targeting specificity of trafficking vesicles by combinatorial interaction with tethering factors. *Nat. Commun.* **10**, 10.1038/s41467-019-09617-9 (2019).
25. Du, Y. et al. A possible role of vps13b in the formation of golgi-lipid droplet contacts associating with the ER. *Contact* **6**, 10.1177/25152564231195718 (2023).
26. Hancock-Cerutti, W. et al. ER-lysosome lipid transfer protein VPS13C/PARK23 prevents aberrant mtDNA-dependent STING signaling. *Journal of Cell Biology* **221**, e202106046 (2022).
27. Guillén-Samander, A. et al. VPS13D bridges the ER to mitochondria and peroxisomes via Miro. *Journal of Cell Biology* **220**, e202010004 (2021).
28. Cai, S. et al. In situ architecture of the lipid transport protein VPS13C at ER–lysosome membrane contacts. *Proc. Natl. Acad. Sci. USA* **119**, e2203769119 (2022).
29. Lee, Y. K. et al. Cohen syndrome patient ipsc-derived neurospheres and forebrain-like glutamatergic neurons reveal reduced proliferation of neural progenitor cells and altered expression of synapse genes. *J Clin Med* **9**, 1–20 (2020).
30. Arasaki, K. et al. A Role for the ancient SNARE syntaxin 17 in regulating mitochondrial division. *Dev Cell* **32**, 304–317 (2015).
31. Tang, Z. et al. TOM40 Targets Atg2 to Mitochondria-Associated ER Membranes for Phagophore Expansion. *Cell Rep* **28**, 1744–1757.e5 (2019).
32. Velikkakath, A. K. G., Nishimura, T., Oita, E., Ishihara, N. & Mizushima, N. Mammalian Atg2 proteins are essential for autophagosome formation and important for regulation of size and distribution of lipid droplets. *Mol Biol Cell* **23**, 896–909 (2012).
33. Ugur, B., Hancock-Cerutti, W., Leonzino, M. & De Camilli, P. Role of VPS13, a protein with similarity to ATG2, in physiology and disease. *Curr Opin Genet Dev* **65**, 61–68 (2020).
34. de Brito, O. M. & Scorrano, L. Mitofusin 2 tethers endoplasmic reticulum to mitochondria. *Nature* **456**, 605–610 (2008).
35. Filadi, R. et al. Mitofusin 2 ablation increases endoplasmic reticulum–mitochondria coupling. *Proc. Natl. Acad. Sci. USA* **112**, E2174–E2181 (2015).
36. Söderberg, O. et al. Direct observation of individual endogenous protein complexes in situ by proximity ligation. *Nat Methods* **3**, 995–1000 (2006).
37. Youle, R. J. & Narendra, D. P. Mechanisms of mitophagy. *Nat Rev Mol Cell Biol* **12**, 9–14 (2011).
38. Palikaras, K., Lionaki, E. & Tavernarakis, N. Mechanisms of mitophagy in cellular homeostasis, physiology and pathology. *Nat Cell Biol* **20**, 1013–1022 (2018).
39. Nagashima, S. et al. Golgi-derived PI(4)P-containing vesicles drive late steps of mitochondrial division. *Science (1979)* **367**, 1366–1371 (2020).
40. Ajiki, M. et al. ORP9-PH domain-based fluorescent reporters for visualizing phosphatidylinositol 4-phosphate dynamics in living cells. *RSC Chem Biol* **5**, 544–555 (2024).
41. Cohen, M. M., Hall, B. D., Smith, D. W., Graham, C. B. & Lampert, K. J. A new syndrome with hypotonia, obesity, mental deficiency, and facial, oral, ocular, and limb anomalies. *J Pediatr* **83**, 280–284 (1973).
42. Nlm Citation,:, Wang, H., Falk, M. J. & Wensel, C. *Cohen Syndrome*. (2006).
43. Seifert, W. et al. Mutational spectrum of COH1 and clinical heterogeneity in Cohen syndrome. *J Med Genet* **43**, e22–e22 (2006).
44. Chen, S. et al. VPS13A and VPS13C influence lipid droplet abundance. *Contact* **5**, 10.1177/25152564221125613 (2022).
45. Duan, X. et al. PI4P-containing vesicles from golgi contribute to mitochondrial division by coordinating with polymerized actin. *Int J Mol Sci* **24**, 6593 (2023).
46. Burman, J. L. et al. Mitochondrial fission facilitates the selective mitophagy of protein aggregates. *Journal of Cell Biology* **216**, 3231–3247 (2017).
47. Nguyen, T. N. et al. Atg8 family LC3/GAB ARAP proteins are crucial for autophagosome-lysosome fusion but not autophagosome formation during PINK1/Parkin mitophagy and starvation. *Journal of Cell Biology* **215**, 857–874 (2016).
48. Pickles, S., Vigié, P. & Youle, R. J. Mitophagy and quality control mechanisms in mitochondrial. *Maintenance. Current Biology* **28**, R170–R185 (2018).
49. Okita, K. et al. A more efficient method to generate integration-free human iPS cells. *Nat Methods* **8**, 409–412 (2011).
50. Zhang, Y. et al. Rapid single-step induction of functional neurons from human pluripotent stem cells. *Neuron* **78**, 785–798 (2013).
51. Park, S. W. et al. Monitoring LC3- or GABARAP-positive autophagic membranes using modified RavZ-based probes. *Sci Rep* **9**, 16593 (2019).
52. Wieckowski, M. R. M. R., Giorgi, C., Lebiedzinska, M., Duszynski, J. & Pinton, P. Isolation of mitochondria-associated membranes and mitochondria from animal tissues and cells. *Nat Protoc* **4**, 1582–1590 (2009).

Acknowledgements

The work was supported by the Science Research Center Program of the National Research Foundation NRF (RS-2020-NR049540); Basic research program of the NRF (RS-2023-NR077176); the Bio & Medical Technology Development Program through the National Research Foundation of Korea (NRF) funded by the Ministry of Science and ICT (RS-2025-02262991); the National Research Foundation of Korea (NRF) funded by the Korea government (MSIT) under the Korea–Japan Joint Research Program (RS-2025-00508237); The Regional Innovation System & Education(RISE) program of the Ministry of Education(MOE) and the Daejeon Metropolitan City (2025-RISE-06-013) to J.-A.L. The NRF grant funded by the Ministry of Science and ICT (RS-2023-00218515) to D.-J.J., the Basic Science Research Program through the National Research Foundation of Korea (NRF) funded by the Ministry of Education (RS-2023-00275835) to S.-K.L., and the National Research Foundation of Korea NRF (2022R1A2C1009376) to J.Y.M.

Author contributions

J.-A.L. and D.-J.J. conceptualized and supervised the study, designed the experiments, interpreted the data, and wrote the manuscript. J.-A.L. served as the corresponding author and oversaw all aspects of the project. S.-K.L. designed the experiments, performed the majority of the experiments, analyzed the data, and contributed to writing the manuscript. H.H. performed PLA assays and FRAP analyses, and assisted with immunocytochemistry, immunoblotting, and quantitative data analysis. S.P. performed several biochemical assays and carried out experiments using CS iPSCs and CS iPSC-derived neurons. H.E.L. and J.Y.M. contributed to transmission electron microscopy (TEM) experiments. All authors reviewed the manuscript, provided feedback and revisions, and approved the final version for publication. All authors have given their consent for publication.

Competing interests
The authors declare no competing interests.

Additional information
Supplementary information The online version contains supplementary material available at https://doi.org/10.1038/s41467-025-67445-6.

Correspondence and requests for materials should be addressed to Deok-Jin Jang or Jin-A Lee.

Peer review information *Nature Communications* thanks Sho Suzuki, who co-reviewed with Guillaume Thibault, and the other, anonymous, reviewer(s) for their contribution to the peer review of this work. A peer review file is available.